

Article

X-ray Imaging-Based Void Fraction Measurement in Saturated Flow Boiling Experiments with Seawater Coolant

Seth Eckels, Zayed Ahmed *, Molly Ross, Daniel Franken, Steven Eckels and Hitesh Bindra

Department of Mechanical and Nuclear Engineering, Kansas State University, Manhattan, KS 66506, USA; sethe44@ksu.edu (S.E.); molly199@ksu.edu (M.R.); dfranken@ksu.edu (D.F.); eckels@ksu.edu (S.E.); hbindra@ksu.edu (H.B.)

* Correspondence: zayedahmedz@ksu.edu

Abstract: Recent studies have shown that the presence of dissolved salts in water can exhibit peculiar flow boiling and two-phase flow regimes. Two-phase flow and convective flow boiling are typically characterized with the help of void fraction measurements. To quantitatively improve our understanding of two-phase flow and boiling phenomenon with seawater coolant, void fraction data are needed, which can not be obtained from optical imaging. In this paper, we present experimental void fraction measurements of saturated flow boiling of tap water and seawater using X-ray radiography. X-rays with a maximum energy level of 40 KeV were used for imaging the exit region of the heated test section. At lower heat flux levels, the two phase flow in seawater was bubbly and homogeneous in nature, resulting in higher void fractions as compared to tap water. With an increase in heat flux, the flow regime was similar to slug flow, and void fraction measurements approached similarity with tap water. The predicted pressure drop using the measured void fraction shows good agreement with the measured total pressure drop across the test section, demonstrating the validity of the measurement process.

Keywords: X-ray imaging; flow boiling; seawater; void fraction; flow regimes; pressure drop



Citation: Eckels, S.; Ahmed, Z.; Ross, M.; Franken, D.; Eckels, S.; Bindra, H. X-ray Imaging Based Void Fraction Measurement in Saturated Flow Boiling Experiments with Seawater Coolant. *Quantum Beam Sci.* **2021**, *5*, 31. <https://doi.org/10.3390/qubs5040031>

Academic Editor: Robert S Bradley

Received: 27 September 2021

Accepted: 9 November 2021

Published: 15 November 2021

Publisher's Note: MDPI stays neutral with regard to jurisdictional claims in published maps and institutional affiliations.



Copyright: © 2021 by the authors. Licensee MDPI, Basel, Switzerland. This article is an open access article distributed under the terms and conditions of the Creative Commons Attribution (CC BY) license (<https://creativecommons.org/licenses/by/4.0/>).

1. Introduction

In loss of coolant accidents, it is sometimes necessary for reactor cores to be flooded with raw water or seawater from adjacent large bodies of water [1,2]. Understanding the influence of raw water emergency injection on the ability to maintain long-term core cooling is critical for safety analysis. During the Fukushima accidents, large volumes of seawater were injected directly into the nuclear reactors in an effort to cool the reactor cores and stabilize the thermal response. The main problem with raw or seawater injection is that, because of nucleate boiling in the core, dissolved salts could precipitate out from the solution and onto the surface of the fuel pins or within the pores in a debris bed. The deposited salts degrade heat transfer rates and cause restrictions in the coolant flow path, thereby leading to a deterioration in coolability. There have been various theories and hypotheses to explain this behavior [3–6], fundamentally. While there have been fundamental investigations aimed at developing our understanding of salt crystallization or deposition under boiling, the more practical scenarios for understanding the effect of crystallization or deposition fouling on heat transfer have involved empirical studies on a large scale. To fully understand and correlate the mutually-coupled role of dissolved salts and heat transfer on the overall scale formation—which in turn affects the coolability—carefully-controlled experiments with high-fidelity data on flow boiling and two-phase flow are needed. This paper presents the findings from void fraction measurements during flow boiling in an annular test section and comparisons are presented between seawater and tap water.

In seawater undergoing nucleate boiling, the dissolved constituents do not evaporate as their solvent does near the nucleate boiling locations on nuclear fuel rods. Because of

large localized changes in the volume fraction during the liquid-to-vapor transition, the local salt concentration can reach very high levels unless there is extremely high diffusivity. This can cause the salts to precipitate if the concentration exceeds the solubility limit. Some recent studies show a considerable effect of salt precipitation from artificial seawater onto fuel rods. In this work, an experimental flow-boiling loop is able to conduct experiments with a wide range of heat fluxes and seawater or tap water coolant inlet conditions. The annular test section heated by a coaxial cartridge electrical heater was cooled with artificial seawater. Void fraction and pressure drop measurements are obtained to understand the differences in saturated flow boiling characteristics between seawater and normal water cooled experiments. Previously, natural circulation and sub-cooled boiling studies were conducted using the same artificial seawater coolant [7,8]. Our motivation for the current, more controlled and X-ray monitored saturated flow boiling study was prompted by the two-phase flow differences observed that can be attributed to hydrodynamic and thermodynamic differences in seawater and tap water flow boiling characteristics.

The differences in the hydrodynamic properties of seawater and distilled water are listed in Table 1. These values are important to compare as the hydrodynamics will determine many of the characteristic flow behaviors. The influence of the hydrodynamic properties can be seen in pressure drop, bubble behavior, and flow stability. The properties for seawater were taken as a pure mixture, where the values of the salts and pure water were averaged to get the values on a per mass basis.

Table 1. Seawater and deionized water properties at 60 °C and atmospheric pressure.

Property	Seawater [8]	Deionized Water	Ratios
Density (kg/m ³)	1008.9	983.3	1.026
Dynamic Viscosity (Pa·s)	5.07×10^{-4}	4.67×10^{-4}	1.089
Surface Tension (mN/m)	67.44	66.24	1.018
Kinematic Viscosity (m ² /s)	5.04×10^{-7}	4.74×10^{-7}	1.063

The thermodynamic properties influence the amount of vapor generation, saturation temperature, wall superheat, and other temperature-related properties. A few reference properties are in Table 2. The inlet enthalpy was taken at a temperature of 60 °C, while the saturation enthalpy was taken at 120.2 °C, which is the saturation temperature of deionized water at 200 kPa absolute. As mentioned previously, the properties from the tables are taken as a mixture average on a per mass basis.

Table 2. Various thermodynamic properties.

Property	Seawater [8]	Deionized Water	Ratios
Latent Heat of Vaporization (kJ/kg)	2122.9	2201.6	0.964
Inlet Enthalpy (kJ/kg)	240.1	251.3	0.956
Saturation Enthalpy (kJ/kg)	484.6	504.4	0.961
Specific Heat Capacity (kJ/kgK)	4.014	4.183	0.960
Thermal Conductivity (W/mK)	0.681	0.682	0.999
Boiling Point Elevation (°C)	0.585	N/A	N/A

A vital difference between the two fluids is the enthalpy and latent heat of vaporization values. The inlet enthalpy and saturation enthalpy values for seawater are lower than for deionized water. Additionally, the difference between the inlet enthalpy and saturation enthalpy values are lower for seawater than they are for deionized water. This difference indicates that seawater would reach a saturation condition at a lower heat input value than deionized water. The lower saturation enthalpy and latent heat of vaporization for seawater would lead to an increase in vapor generation when compared to deionized water. However, this is misleading as the values for enthalpy and latent heat of vaporization are taken on a per unit mass basis. The dissolved salts present in the seawater would effectively reduce the amount of water present per unit mass of seawater. Due to density differences, if both seawater and deionized water had the same mass flow rate, the actual amount of water flow during flow boiling would be lower in the seawater.

In previous experiments, an evolution of the heat transfer characteristics on the heating rod were measured during long term steady state experiments. A wall temperature increase was observed over the course of the experiment due to heat transfer degradation on the surface of the fuel rod. Nucleation sites form and remiss as the boiling front slowly changes over time. Flow regimes in the riser section went from bubbly to churn flow with slugs over several hours of experiments. These changes are postulated to happen due to the salt concentration changes in the coolant over time as salt deposits on the rod and around the system. These consequences can have a significant impact on the local void fraction in the channel. Analyzing the void fraction and its evolution over time could provide further insight into how the seawater effects overall performance.

The use of X-ray/neutron imaging has been previously shown to work well for locations with limited optical access [9–13]. X-ray and neutron imaging has proven to be highly useful for flow imaging in industrial piping applications where there is little to no optical access. They can also be used in transparent tubes/pipes to directly quantify the volume fractions of a phase in a multiphase mixture. In our previous reports, we utilized high-speed imaging to capture flow regimes and bubble formation data. We found some interesting flow regime behavior with seawater due to the presence of small bubbles. Those qualitative observations using optical imaging were helpful in explaining the pressure drop and mass-flow behavior of the system, but void fraction estimates are needed for validation purposes. There are two main objectives of the experiments and results presented in this work: to measure and compare void fraction estimates for seawater and tap water; and to obtain the time-resolved evolution of void fraction with seawater. The following sections describe the experimental setup and the methodology used to measure the void fractions and the corresponding thermal-hydraulic parameters. The results of the investigation are discussed, followed by the future scope of this work.

2. Methodology

2.1. Experimental Setup

A schematic of the experimental setup is shown in Figure 1. In the closed system, the fluid is circulated in the loop with the help of a centrifugal pump capable of reaching Reynolds numbers of close to 15,000. The sheathed electric heater mimics an intact fuel rod and thermocouples embedded into the heater allow for wall temperature measurements. The heater power is controlled by a variac and has a maximum output of 2.6 kW. The hot fluid exiting the test section enters the riser section followed by the heat exchanger/condenser unit of the test loop. The fluid flows at a fixed rate of 1.26 L/s through a heat transfer area of 0.25 m² on the secondary side of the heat exchanger.

The test section consists of a 1.2 m tall borosilicate glass tube with an inner diameter of 2.54 cm. The tube encases a cartridge heater 0.6 m tall with an outer diameter of 1.58 cm. The hydraulic diameter of the annular flow region within the test section is 0.96 cm. Various instruments are placed throughout the loop to record relevant thermal hydraulic parameters. The flowrate is measured by means of a Coriolis flowmeter. RTD temperature probes and pressure transducers are located at the inlet and outlet of the test section. The

voltage and current going into the heater are measured to estimate the total power being transferred by a DC power supply. The uncertainties associated with various instruments are shown in Table 3.

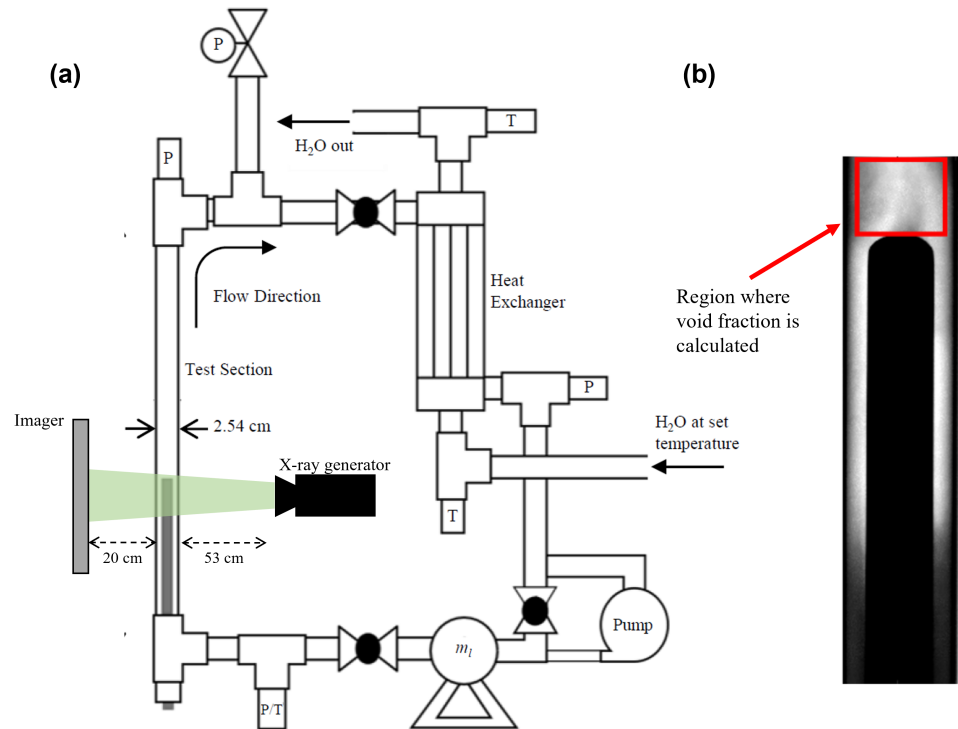


Figure 1. (a) Diagram schematic of the experimental setup. (b) Example X-ray image as obtained from the X-ray imaging system during flow boiling experiments.

Table 3. Instrumentation error.

Instrumentation	Error
Emerson Coriolis Flow Meter	± 0.03 g/s
Emerson Conductivity Probe	$\pm 4\%$ of reading
Type K Thermocouples	± 2.2 °C
Pressure Transducers (0–206.8 kPa abs.)	$\pm 0.4\%$ FS
Variac Power Output	± 15 W

The X-ray generator used in the experiments is capable of producing an output power of 2.8 kW and has a current range of 0.4–100 mA and an energy range of 40–120 kV. The X-ray collimator tube is capable of generating an X-ray field with dimensions: min. 5 cm \times 5 cm at 1 m SID and max. 40 cm \times 40 cm at 75 cm. The actual settings used for conducting these experiments were: 20 mAs and 40 kV. The generator was positioned at an elevation to view the top portions of the annular test section and the beginning of the riser section.

To image the transmitted beam through the test section, a high-speed neutron or X-ray imaging camera (XRD 0822 AO/AP) with a Gadox scintillator was used. Some of the features of the neutron or X-ray imaging camera are: real time imaging; 1 megapixel; 0.2 mm pixel pitch; 64,000 gray levels; compatible with X-rays from 20 KeV to 15 MeV; up to 100 frames per second; and gigabit Ethernet interface.

2.2. Experimental Procedure

Two overall objectives of this study were to estimate the differences in the void fraction between artificial seawater and tap water cooled systems and to observe the void fraction evolution with time. The next goal was to obtain values on how the void fraction changes with seawater as salts deposit along the rod and throughout the system during 3 h after achieving the first quasi-steady thermal conditions. For the comparative study, the experimental tests as depicted in Table 4 were conducted with tap water. Then, artificial seawater was created using Instant Ocean, a commercially available product. The solution was made at 3.5% wt and was allowed to aerate for at least 12 h before use to ensure that the solution was at an oxygen and carbon dioxide equilibrium.

Table 4. Experimental flow conditions.

Test Number	\dot{m}_l (g/s)	T_{li} (°C)	Q (W)	P (kPa)	Salinity (g/L)
1	10	72.5	1600	128	35
2	10	72.5	1800	128	35
3	10	72.5	2000	128	35

The system was filled with water and the pump turned on with all the valves open, allowing for a flow of 180 g/s through the system. Fluid was brought up to working temperature and allowed to flow single-phase around the system to bring the fittings up to temperature. This allowed the seawater to reach a steady state quicker. Once the system was at the correct inlet temperature and pressure, the heater was turned on to the desired power level. Adjustments to reach steady state were made using the pressure relief valve at the top of the system and by controlling the temperature in the heat exchanger. Flow was considered to be in steady state when it would remain within operating limits for ten minutes and the variability at the inlet was within ± 0.5 °C, ± 1 psi, and ± 0.5 g/s.

Once at steady state, the first round of X-ray images were recorded. This process was the same for tap water, and these initial steady state comparisons can be seen in the charts below. Over time, it was shown that for tap water there was no change in the average pixel values of X-ray images and the system was maintained at an almost true thermal steady state. For seawater cases, the images were taken at every one hour interval throughout the duration of the experiments. After the end of each experiment, the heater was turned off and flow was stopped. X-ray images were recorded with test section and the system completely filled with water. In the next step, the system was drained and X-ray images of the empty (air-filled) test section were recorded. These X-ray images of the air-filled and water-filled test section were used to obtain the void fraction estimates during boiling or two-phase flow experiments. The void fraction was calculated in a 2.54 cm \times 2.54 cm region located above the tip of the heater (see red box in Figure 1b).

2.3. Estimating Void Fractions from X-ray Images

The attenuation of X-rays through materials follows the Beer–Lambert law, as shown by:

$$\frac{I}{I_0} = e^{-\mu_f t} \quad (1)$$

Since the detector pixel value is directly proportional to the X-ray fluence incident on the detector, the pixel value is given by the equation:

$$P_f = C e^{-\mu_f t} \quad (2)$$

The subscript f denotes a particular experimental test run. Similarly, for air (same as void region) and water filled reference cases, the pixel relationships are $P_a = C e^{-\mu_a t}$ and $P_w = C e^{-\mu_w t}$, respectively. The attenuation coefficient for fluid comprising two phases

(vapor and water), can be assumed to be linearly related to the water or void fraction and is expressed by:

$$\mu_f = \alpha\mu_a + (1 - \alpha)\mu_w \quad (3)$$

Taking the log-transform of the pixel-values, P , and algebraic manipulation, we get:

$$\alpha = \frac{\log(P_f) - \log(P_w)}{\log(P_a) - \log(P_w)} \quad (4)$$

3. Experimental Results

The MATLAB® Image Processing Toolbox was used to analyze on the images. This toolbox converts the '.his' images to '.mat' data files that can then be used to process additional information or perform mathematical operations such as transforms. In order to set the reference scale for the test cases described earlier, the calibration images of the test section were taken with only-air and only-water filled systems, without any fluid motion, on each day of testing. Experiments at three operating test conditions (see Table 4) were conducted by varying the power level and keeping the flow rate, pressure, and inlet temperature constant. Initial tests were conducted with tap water and then the same set of experiments with the same power levels were repeated with seawater, allowing the system to stay at quasi-steady state for three hours. A three-hour window was chosen based upon our previous experience with seawater tests where salt deposits and wall temperature changes reach a plateau after this time period.

Visual inspection of the flow patterns during experiments offers some insight. At lower power levels, a very bubbly foam-like flow occurs in seawater, and it is speculated that the presence of dissolved salts inhibits coalescence and prevents the formation of larger bubbles or slugs. tap water cases show churn or slug flow regimes at all power levels.

3.1. Seawater Cases: Evolving Void Fractions and Flow Regimes

The X-ray images in Figures 2–4 show the evolution of void fraction images over the course of the experiments. The three test cases presented here were performed with different power levels, and all cases show a reduction in void fractions over time. With time, the salt deposits are expected to accumulate on the heater surface and thus ionic concentration in the water will decrease. Over time, the flow evolves from a uniform bubbly flow to a turbulent churn flow. Although this behavior can be seen clearly from visual inspection, X-ray images provide a clear transition from the uniform stable image of fluid phase around the heater test rod to the image of heterogeneous fluid phase with flow instability at the three hour mark. The contour plots here directly depict the void fractions as calculated using the log transform of images. The average values of void fraction based in the snapshots obtained at one hour intervals during three hour tests are reported in Figure 5. At quasi-steady state conditions, i.e., when there is no significant change in system or wall temperatures, the void fraction values observed in seawater decrease as the heater power level increases.

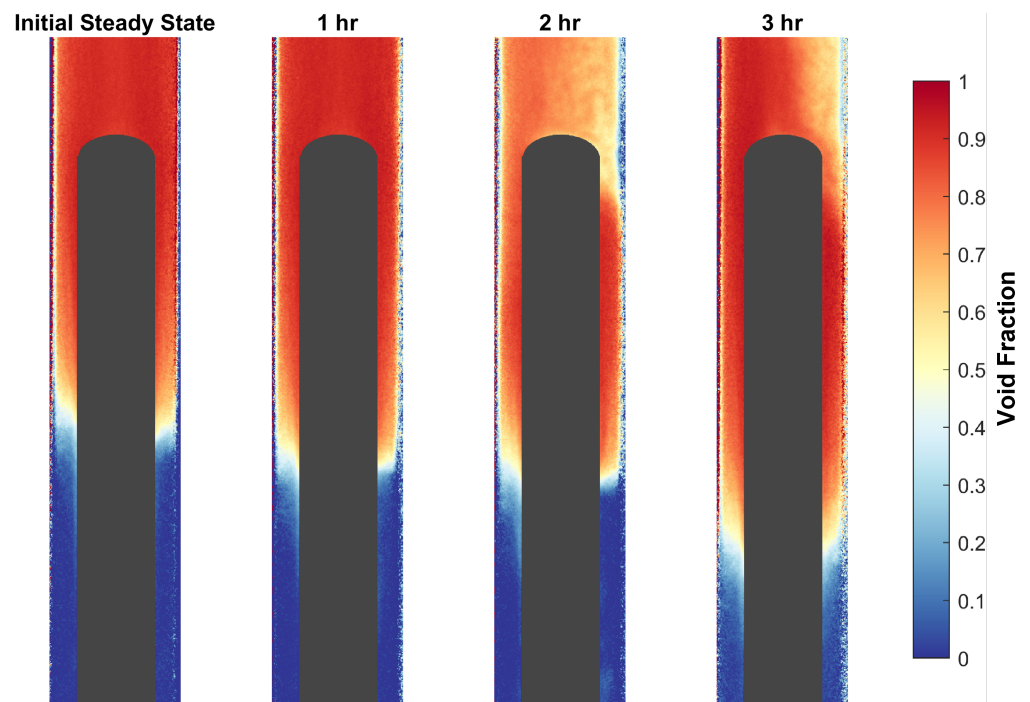


Figure 2. $Q = 1600$ W: Processed void fraction measurements of seawater and their evolution over time.

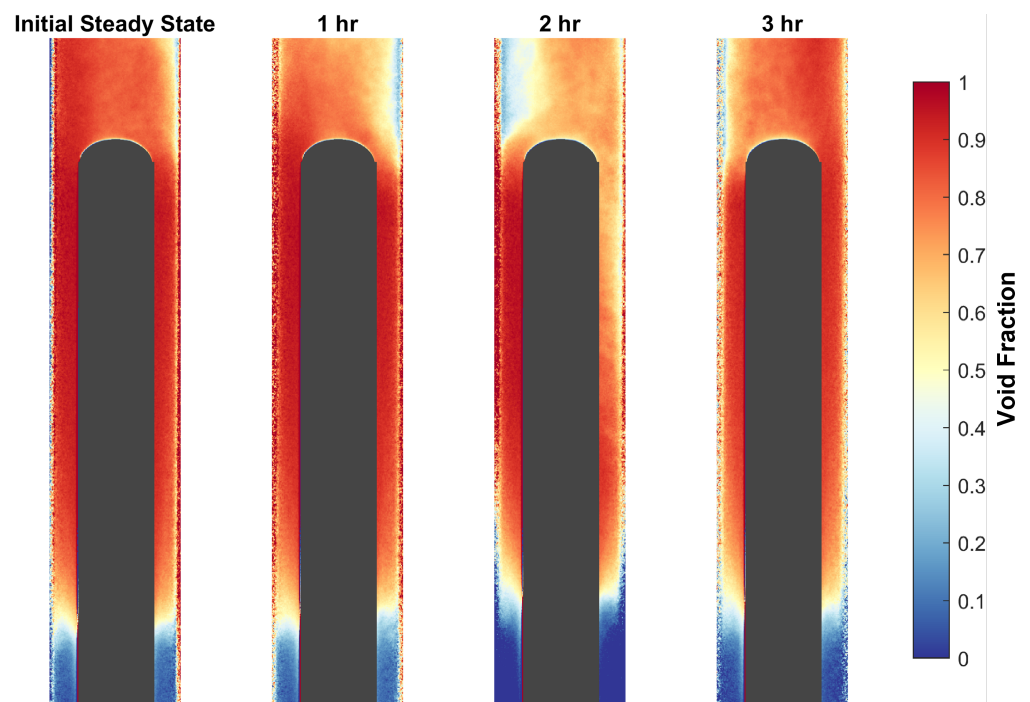


Figure 3. $Q = 1800$ W: Processed void fraction measurements of seawater and their evolution over time.

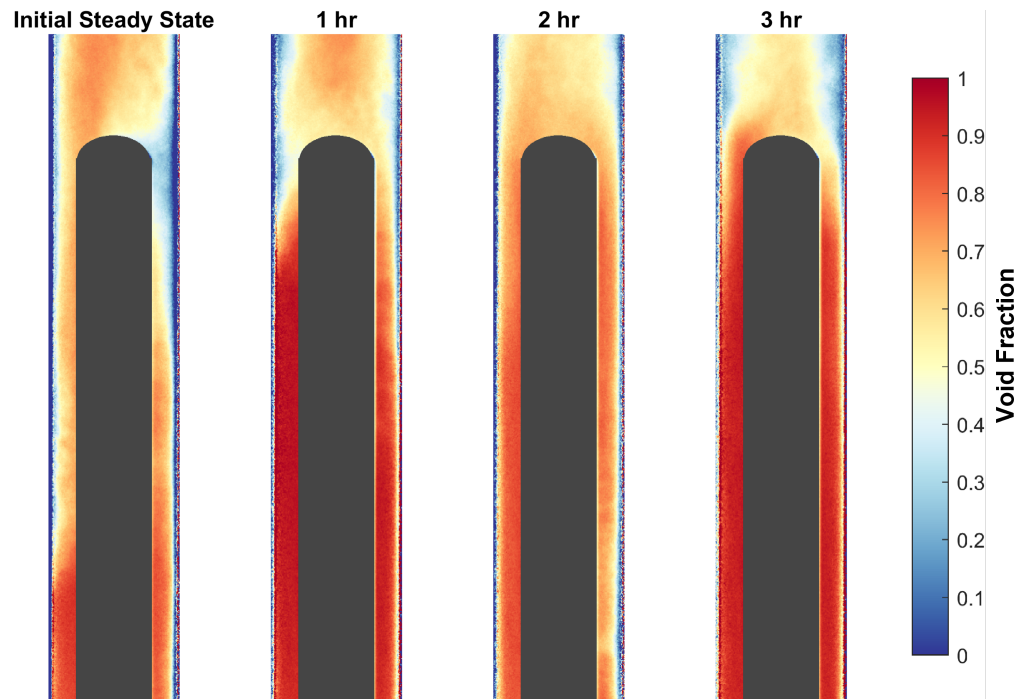


Figure 4. $Q = 2000$ W: Processed void fraction measurements of seawater and their evolution over time.

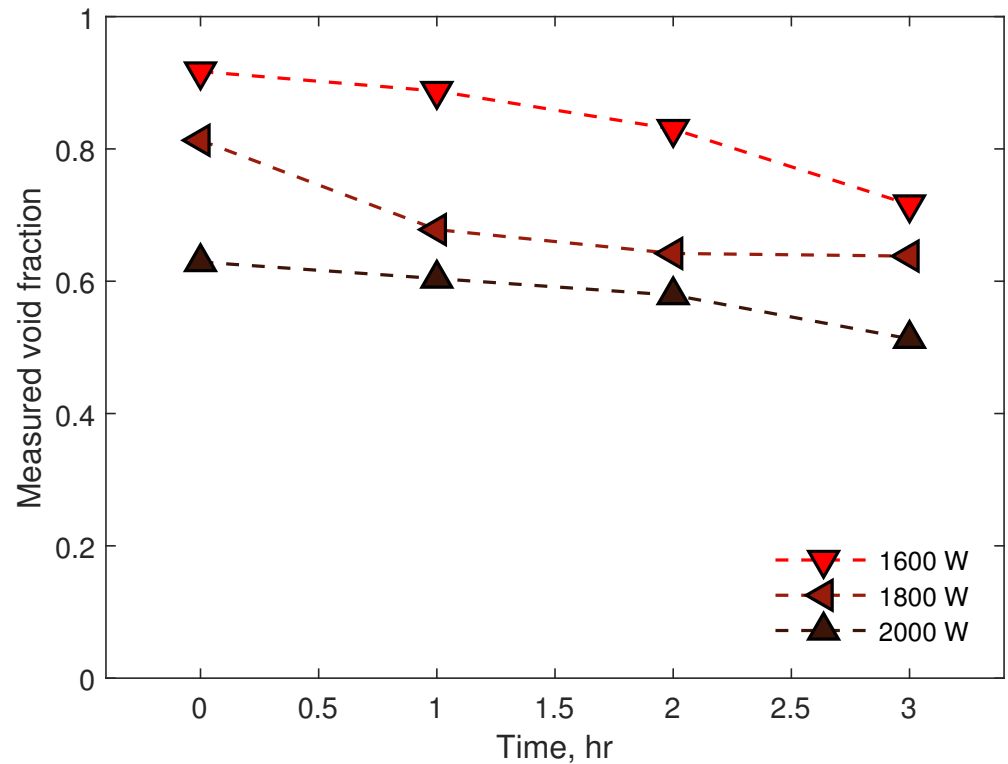


Figure 5. Comparison of the measured void fraction of salt water over time.

3.2. Comparison Between Seawater and Tap Water Cases

Tap water tests were also conducted for three hours but no discernible change in void fraction was recorded. Tap water tests were conducted for power levels ranging from 1400–2000 W at increments of 100 W. Tap water exhibits the opposite trend of increasing void fraction as the power increases.

The comparison between seawater and tap water cases show that as the power level increases, the void fractions observed in tap water cases increase, whereas the effect was the complete opposite in the case of seawater. It is also evident that under all scenarios, tap water shows lower void fraction levels. For all three test cases, i.e., at three different power levels, seawater had a significantly higher void fraction (Figures 6 and 7). This gap became smaller at higher power levels.

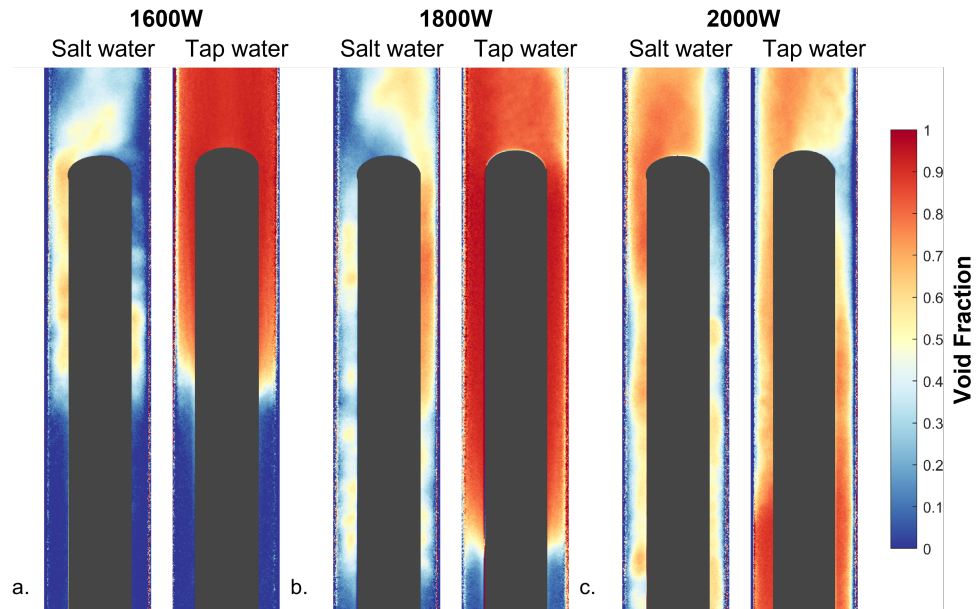


Figure 6. Comparison of void fraction of salt water (left) and tap water (right) at initial steady state conditions for different power levels. (a) 1600 W. (b) 1800 W. (c) 2000 W.

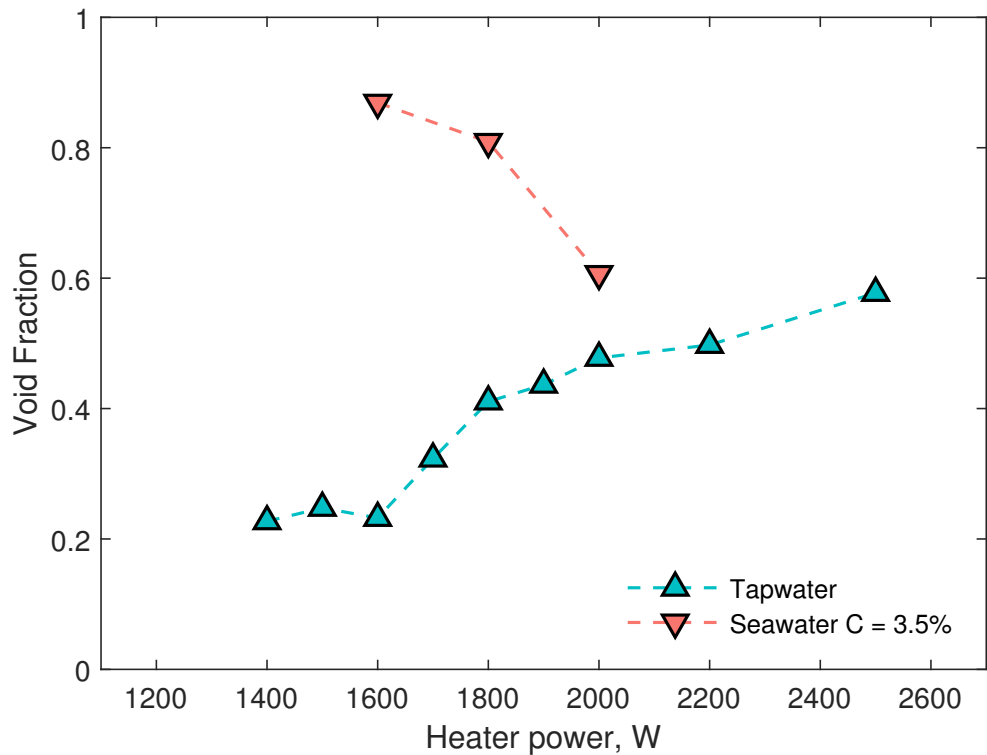


Figure 7. Seawater and tap water void fraction comparisons at different power levels.

4. Discussion

In two-phase flow, the distribution of the gas phase and liquid phase plays an essential role in establishing the pressure drop and heat transfer rate characteristics. The influence of dissolved salts can alter the flow regime and the impact of inhibition of coalescence may shift the distribution of bubbles present towards smaller bubbles. Each flow pattern can be categorized as one of several different types of flow regime. There are two basic categories of two-phase flow regimes that are dependent on the orientation of the flow with respect to the ground—bubbly flow and separated flow regimes.

In the bubbly flow regime, the gas is distributed in a way in which there are many discrete bubbles. The bubbles tend not to coalesce and remain much smaller than the diameter of the pipe. The general shape of the bubbles tends to very spherical while small and slightly non-spherical when larger. This regime is relatively stable with few oscillations. Additionally, this flow is highly homogeneous with mean properties consistent throughout the flow path. The dissolved salts within seawater inhibit coalescence; therefore, it would be expected that seawater in a two-phase flow loop would likely remain in the bubbly flow regime. However, this would compete with the higher surface tension value of seawater, which would suggest larger bubbles and more coalescence. If the inhibition of coalescence is dominant, then this would suggest the flow rate would be expected to be more stable than that of tap water.

Given that the expected vapor production and flow regime may be different between seawater and tap water, it is expected that the pressure drop would then be influenced. The impact of dissolved salts changes the fluid properties in a minor way but affect flow conditions considerably, which makes using conventional pressure drop models possibly unreliable.

In the homogeneous flow model, the total pressure drop over a specific length is a sum of the contributions of the static head, momentum head and the frictional head. The change in static pressure describes the pressure change due to elevation or height differences between the locations being measured. The momentum or acceleration pressure drop takes into consideration the acceleration of the vapor needed to conserve the conservation of mass. Lastly, the frictional pressure drop is used to determine the pressure drop due to friction between the phases and the channel wall. The total pressure drop can then be calculated by taking the sum of each component of the pressure drop as:

$$\left(\frac{dp}{dz}\right)_{total} = \left(\frac{dp}{dz}\right)_{static} + \left(\frac{dp}{dz}\right)_{momentum} + \left(\frac{dp}{dz}\right)_{friction} \quad (5)$$

The static pressure drop gradient is calculated using the void fraction α as:

$$\left(\frac{dp}{dz}\right)_{static} = \rho_H g \quad (6)$$

where ρ_H is the homogeneous density and g is the acceleration due to gravity. The homogeneous density can be calculated using:

$$\rho_H = \rho_l(1 - \alpha_{exp}) + \rho_g \alpha_{exp} \quad (7)$$

where α_{exp} is the experimentally measured void fraction. The momentum pressure drop gradient along the channel length for the total mass flux G is given by:

$$\left(\frac{dp}{dz}\right)_{momentum} = \frac{d(G^2/\rho_H)}{dz} \quad (8)$$

The frictional pressure drop gradient is found through the following equation:

$$\left(\frac{dp}{dz}\right)_{friction} = \frac{2f_{tp}G^2}{\rho_H D_h} \quad (9)$$

where f_{tp} is the two-phase friction factor and D_h is the hydraulic diameter. Here, the Blasius equation was used for f_{tp} , which is given by:

$$f_{tp} = 0.079 \left(\frac{GD_h}{\bar{\mu}} \right)^{-0.25} \quad (10)$$

where μ_{tp} is the two-phase dynamic viscosity, which is a mass-averaged viscosity.

$$\mu_{tp} = x\mu_g + (1-x)\mu_{tp} \quad (11)$$

For the calculations presented here, the experimentally measured void fraction was used in calculating the total pressure drop across the two phase channel. Here it was assumed that there exists a linear variation of thermodynamic vapor quality between the calculated onset of nucleate boiling (ONB) point and the end of the heated section. The flow was assumed to be completely single phase in the region below the ONB point. The results of the total pressure drop obtained from the model described above with the experimentally measured total pressure drop are shown in Figure 8. Pure water shows that the pressure drop from the homogeneous model is a very good match with the experimental observations, even at higher power levels. However, in the case of seawater, a discrepancy is observed between experimental observations and the predictions of the model.

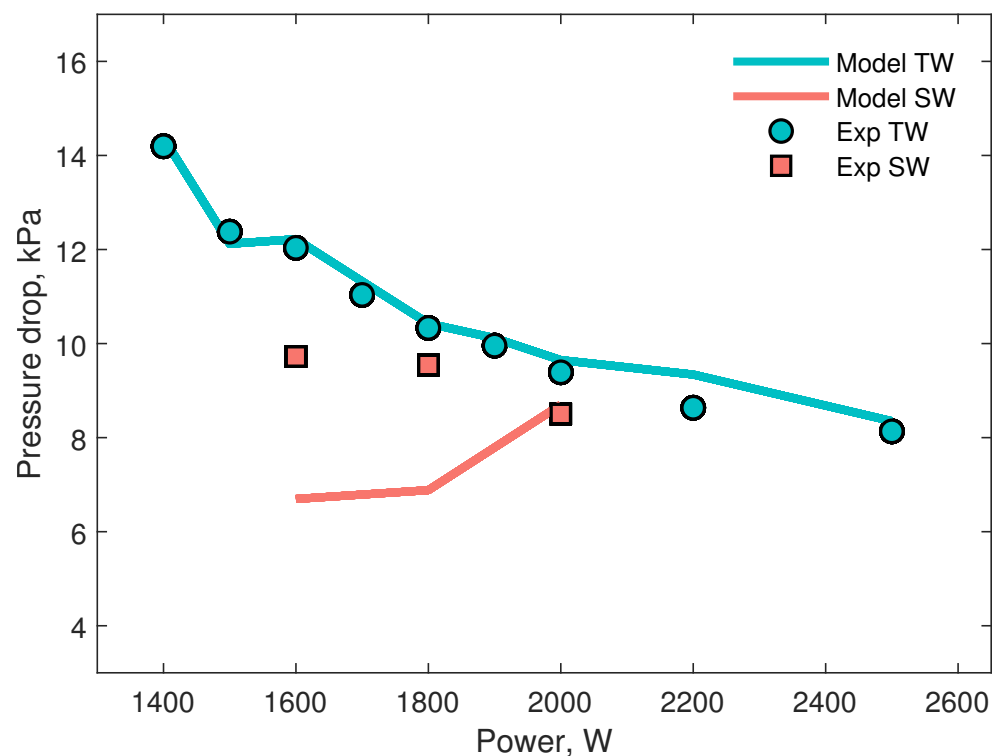


Figure 8. Comparison of total pressure drop with experimental measurements for pure water and sea water.

As discussed previously, the presence of salts in the liquid inhibits bubble coalescence. The various ionic components have an affinity towards the liquid–vapor interface and this concentration of the ionic charges at the interfaces creates a repulsion force between the bubbles, thus preventing them from agglomerating together into a bigger bubble. The presence of salts also reduces the diameter of the bubbles in the two-phase flow. Smaller bubbles do not experience the same buoyancy force to drag force ratio as larger bubbles and therefore move slower in the liquid relative to larger bubbles. This condition can create a separated flow in which the liquid may be moving faster than the bubbles. This can create

high bubble hold up and increase void fraction locally. The higher void fraction reduces the total static pressure head across the test section and therefore leads to a reduced pressure drop with the use of seawater. Further modeling of the ionic charge distribution around a bubble in bubbly flow is needed to accurately account for the presence of salts in the pressure drop calculations.

5. Conclusions

Saturated flow boiling experiments were conducted with seawater forced circulation in the annular test section and a coaxially located electrical cartridge heater in the cylindrical test section. X-ray imaging was used to obtain radiographs of the test section near the exit. The data obtained from these experiments were used to determine void fractions for flow boiling in a vertical annulus. The experimental data show enough contrast in X-ray radiographs to show the difference in void fractions. Tests were conducted to record void fraction data at initial steady state, and then after three hours of maintaining quasi-steady state conditions. These results show the time evolution of the two-phase flow characteristics during the course of the experiment. Seawater showed a significantly higher void fraction at all power levels as compared to tap water. Over three hours, the void fraction in seawater decreases as slugs begin to form and the flow loses its uniform bubbly flow behavior.

The void fraction data measurements were used to estimate pressure drops and rises across the test section. These estimates are compared to the pressure drop measurements obtained from pressure transducers. For tap water and high power level cases of seawater, the pressure drop estimates and measurements are found to be in close agreement. The pressure drop predictions for seawater cases exhibiting the highest void fraction do not match well with our measurements. This may be due to the peculiar bubbly/frothy mixture attributed to a high level of ionic concentrations in seawater, which prohibits coalescence. The model's accuracy can be increased by considering the separate flow effects between the liquid and vapor phases and by taking into account the interaction between the phases. Further research is needed in the field of understanding liquid flow acceleration effects around the bubbly mixture in the test section.

Author Contributions: Writing—original draft preparation, S.E. (Seth Eckels) and Z.A.; writing—review and editing, S.E. (Steven Eckels); methodology, M.R. and D.F.; data curation, Z.A. and M.R.; supervision, H.B. and S.E. (Steven Eckels); investigation, S.E. (Seth Eckels) and Z.A.; formal analysis, Z.A. and M.R.; software, M.R.; conceptualization, D.F.; project administration, S.E. (Steven Eckels) and H.B. All authors have read and agreed to the published version of the manuscript.

Funding: The work presented was supported by the U.S. Department of Energy, Nuclear Energy University Program under Award DE-NE0008690 and DE-NE0008498. The author Molly Ross acknowledges the support of NRC fellowship program.

Data Availability Statement: Not applicable.

Conflicts of Interest: The authors declare no conflicts of interest.

References

1. Li, G.; Zhang, J.; Qiu, B.; Liu, M.; Yan, J. MELCOR modeling and sensitivity analysis of Fukushima Daiichi unit 2 accident considering the latest TEPCO investigations. *Ann. Nucl. Energy* **2018**, *112*, 364–373. [[CrossRef](#)]
2. Liu, W.; Nagatake, T.; Takase, K.; Yoshida, H.; Nagase, F. Research of Seawater Effects on Thermal-Hydraulic Behavior at Severe Accident: 1—Research Plan and Results of Preliminary Experiments. In Proceedings of the 21st International Conference on Nuclear Engineering, Chengdu, China, 29 July–2 August 2013; Volume 55812, p. V004T09A108.
3. Hall, R.E. A System of Boiler Water Treatment Based on Chemical Equilibrium. *Ind. Eng. Chem.* **1925**, *17*, 283–290. [[CrossRef](#)]
4. Freeborn, J.; Lewis, D. Initiation of boiler scale formation. *J. Mech. Eng. Sci.* **1962**, *4*, 46–52. [[CrossRef](#)]
5. Hospeti, N.B.; Mesler, R.B. Deposits formed beneath bubbles during nucleate boiling of radioactive calcium sulfate solutions. *AIChE J.* **1965**, *11*, 662–665. [[CrossRef](#)]
6. Müller-Steinhagen, H.; Malayeri, M.; Watkinson, A. Fouling of heat exchangers—new approaches to solve an old problem. *Heat Transf. Eng.* **2005**, *26*, 1–4. [[CrossRef](#)]
7. Ahmed, Z.; Eckels, S.; Eckels, S.J.; Bindra, H. Forced Convective Boiling in a Vertical Annular Test Section With Seawater Coolant. *J. Nucl. Eng. Radiat. Sci.* **2021**, *7*, 031405. [[CrossRef](#)]

8. Franken, D.; Ahmed, Z.; Eckels, S.; Eckels, S.; Bindra, H. Impact of dissolved salts on two-phase flow and boiling heat transfer in a natural circulation loop. *Chem. Eng. Sci.* **2019**, *206*, 463–470. [[CrossRef](#)]
9. Kojo, R.; Hotta, A.; Furuya, M.; Akiba, M.; Hoshi, H. Detailed Observation of Seawater Precipitation With 5×5 Mockup Fuel Bundle Based on X-ray Computed Tomography Technique. In Proceedings of the 22nd International Conference on Nuclear Engineering, Prague, Czech Republic, 7–11 July 2014; Volume 45967, p. V006T15A008.
10. Tebianian, S.; Ellis, N.; Lettieri, P.; Grace, J.R. X-ray imaging for flow characterization and investigation of invasive probe interference in travelling fluidized bed. *Chem. Eng. Res. Des.* **2015**, *104*, 191–202. [[CrossRef](#)]
11. Balaskó, M.; Hózer, Z.; Maróti, L.; Windberg, P. X-ray radiography inspection of core model of the CODEX AIT-2 facility. In Proceedings of the International Conference on Nuclear Energy in Central Europe 99, Portoroz, Slovenia, 6–9 September 1999; pp. 763–770.
12. Ito, D.; Saito, Y. Visualization of bubble behavior in a packed bed of spheres using neutron radiography. *Phys. Procedia* **2015**, *69*, 593–598. [[CrossRef](#)]
13. Ross, M.; van Bergeijk, A.; Cebula, A.; Eckels, S.; Bindra, H. Neutron Imaging of Percolating Hydraulic Flow Through a Simulated Debris Bed. In *Transactions of American Nuclear Society*; American Nuclear Society: La Grange Park, IL, USA, 2018; Volume 119.